Chromatin arranges in chains of mesoscale domains with nanoscale functional topography independent of cohesin

Ezequiel Miron[1†], Roel Oldenkamp[1†], Jill M. Brown[2], David M. S. Pinto[3], C. Shan Xu[4], Ana R. Faria[1], Haitham A. Shaban[5], James D. P. Rhodes[1], Cassandravictoria Innocent[1‡], Sara de Ornellas[2], Harald F. Hess[4], Veronica Buckle[2], Lothar Schermelleh[1,3*]

[1]Department of Biochemistry, University of Oxford, Oxford OX1 3QU, United Kingdom

[2]MRC Weatherall Institute of Molecular Medicine, Haematology Unit, University of Oxford, Oxford OX3 9DS, United Kingdom

[3]Micron Oxford Advanced Bioimaging Unit, University of Oxford, Oxford OX1 3QU, United Kingdom

[4]Janelia Research Campus, Howard Hughes Medical Institute, Ashburn, VA 20147, USA

[5]Spectroscopy Department, Physics Division, National Research Centre, 12622 Dokki, Cairo, Egypt

*Correspondence to: lothar.schermelleh@bioch.ox.ac.uk

†Present address: Division of Gene Regulation, Netherlands Cancer Institute, Plesmanlaan 121, 1066 CX Amsterdam, The Netherlands

‡ Current address: Neurology Department, Harvard Medical School, Boston Children's Hospital, 300 Longwood Ave, Boston MA 02115, USA

ABSTRACT

Three-dimensional (3D) chromatin organization plays a key role in regulating mammalian genome function, however many of its physical features at the single-cell level remain underexplored. Here we use 3D super-resolution and scanning electron microscopy to analyze structural and functional nuclear organization in somatic cells. We identify linked chromatin domains (CDs) composed of irregular ~200-300-nm-wide aggregates of nucleosomes that can overlap with individual topologically associating domains and are distinct from a surrounding RNA-populated interchromatin region. High-content mapping uncovers confinement of cohesin and active histone modifications to surfaces and enrichment of repressive modifications towards the core of CDs in both hetero- and euchromatic regions. This nanoscale functional topography is temporarily relaxed in post-replicative chromatin, but remarkably persists after ablation of cohesin. Our findings establish CDs as physical and functional modules of mesoscale genome organization.

INTRODUCTION

The genome in mammalian cell nuclei is hierarchically organized at various scales correlating with diverse genomic functions (*1*, *2*). At the base pair to kilobase pair level, DNA is wrapped around core histones to create nucleosomes (*3*). At the 100 Mb scale, entire chromosomes harbor distinct territories within the nucleus with transcriptionally active euchromatic and inactive heterochromatic segments tending to segregate into specific nuclear sub-regions (*4*). Local chromatin organization ranging from several kb to 100 Mb ('mesoscale') remains poorly understood (*5*). Advances in next-generation sequencing-based chromosome conformation capturing methods (3C/Hi-C) have revealed partitioning into several hundred kb to a few Mb-sized topologically associating domains (TADs) (*6*, *7*). TADs are genomic segments with higher intra-TAD contacts compared to inter-TAD contacts. At higher levels of organization, TADs group into ~10-20 Mb genomic A- and B-compartments. A-compartments denote DNase I sensitive, transcriptionally active 'open' chromatin and B-compartments denote transcriptionally repressed, 'closed' chromatin (*8*). Compartments are generally correlated with euchromatin or heterochromatin, nuclear interior or lamina/nucleolar contacts for A- and B-compartments, respectively (*9*).

A key regulator in TAD organization is CCCTC-binding factor (CTCF), which binds to convergently oriented recognition sequences that flank TADs, and which define TAD boundaries at the linear genomic (1D) scale (*10*). Deletion of genomic TAD boundaries leads to aberrant transcriptional output (*11*). Co-occurrence of the ring-shaped cohesin complex at CTCF binding sites suggest a regulatory role for cohesin in shaping TAD structures, possibly through a loop extrusion mechanism (*12*, *13*). Accordingly, loss of cohesin function leads to an erasure of TAD signatures on Hi-C interaction maps (*14*).

Whereas the linear genomic size of TADs is defined, their spatiotemporal organization is underexplored. Single-cell Hi-C and more recent microscopy-based approaches using fluorescence *in situ* hybridization (FISH) of TAD-based regions have observed a high degree of stochasticity and heterogeneity in chromatin conformations in fixed cells (*15*–*19*). Despite such advances in imaging single TADs, it is still unclear whether TADs always form a single physical entity, how they relate to adjacent nuclear compartments and how active and silenced chromatin is distributed at TAD scales.

In silico simulations of chromatin as a melted polymer suggest that the charged properties of modified histone tails alter the compaction status of such chromatin domains (*20*), which was more recently supported by single molecule imaging experiments (*21*). This model explains the increase in the physical size of epigenetically active domains compared to epigenetically inactive domains (*22*). Decreased protein accessibility with increasing chromatin density may allow size differences between small transcription factors (TFs) and large nuclear macro-complexes, such as the transcription machinery, to be exploited as a mechanism of transcriptional control (*23*).

Here we use quantitative 3D super-resolution imaging of both fixed and live samples, complemented by 3D electron microscopy of cryo-preserved samples, to establish chromatin domains (CDs) as TAD-sized irregularly-shaped dense nucleosomal aggregates in the size range of ~200-300 nm. CDs are linked sequentially in a 3D curvilinear arrangement to form a distinct reticular network that is separated by a relatively wide RNA-filled interchromatin space. We apply a novel high-throughput image analysis pipeline for 3D-SIM data to spatially map functional markers, such as structural proteins, histone modifications and RNA

polymerase II (RNAPII). We describe for the first time at physically relevant nanometer scale distinct volumes or zones of genome function in the context of CDs. This organization is independent of cohesin, establishing CDs as functional and physical modules of mesoscale genome organization in mouse and human somatic cells.

RESULTS

Chromatin arranges in coherently moving sub-micrometer domains, distinct from an RNA-occupied interchromatin compartment

The study of <1 Mb chromatin domain topologies in single cells *in situ* and *in vivo* has long been hindered, because they fall beyond the diffraction limit of light microscopy. Advances in super-resolution microscopy now put such structures within visual reach (*18*, *24*). 3D structured illumination microscopy (3D-SIM) enables fast multicolor 3D acquisition of whole cells with 8-fold higher volumetric resolution and strongly enhanced contrast compared to conventional fluorescence microscopy (*25*). Previous 3D-SIM studies resolved 4′,6-diamidino-2-phenylindole (DAPI)-stained chromatin in mammalian somatic cells as an intricate sponge-like structure, juxtaposed to an interchromatin compartment (IC) of no detectable chromatin that ends in channels leading to nuclear pores (Fig. 1A) (*26–28*). Using rigorously quality-controlled 3D-SIM (Methods, Fig. S1A) in mouse (C127) and human (HeLa) somatic cells, we observe chromatin as a chain-like reticular structure of distinct nodes or chromatin domains (CDs) of variable diameters in the range of a few 100 nm, hereafter referred to as CD chains. DNA staining with either DAPI or SYTOX Green both show the same sponge-like pattern, with the exception of relative brighter chromocenter intensity in DAPI-stained mouse cell nuclei owing to its AT-base preference (Figs. 1A and S1A). Control experiments in HeLa cells stably expressing histone H2B-GFP showed a near complete co-localization of H2B-GFP and DNA staining (Fig. S1B). Live cell 3D-SIM imaging (Methods) confirms the presence of a CD chain – IC arrangement *in vivo* (Fig. S1C) and unveiled a highly dynamic behavior of CD features over different observation periods and time intervals (Fig. S2, Movies S1-S3). Furthermore, quantitative flow field analysis (*29*) (Methods, Fig. S2C, Movie S4) reveals localized spatially coherent chromatin motion, i.e. fields with same motion direction. These properties are consistent with mechanically-coupled viscoelastic droplet-like domains (*29*, *30*), or 'blobs'.

We next sought to better understand the content of the relatively wide IC space separating these domains. Considering RNA transcripts as a prime candidate, we performed an extended 5-ethynyluridine (EU) pulse labelling to detect all transcribed RNAs (*31*). We observed a striking enrichment of bulk RNA in the IC space including nucleoli and nuclear pore channels, and almost mutual exclusion with DAPI-stained chromatin (Fig. 1B, C). Line profiles through a representative euchromatic region of the nuclear interior highlight DNA domains in the size range of 200-300 nm alternating with the RNA-containing IC space of similar dimension (Fig. 1D).

The lateral resolution of our 3D-SIM imaging approach is limited to ~110 nm in the green emission range (Fig. S1A). To test if the observed nodal pattern of chromatin derives from structures at the molecular scale, we made use of high-resolution focused ion beam scanning electron microscopy (FIB-SEM). This approach allows imaging of entire nuclear volumes at 4 nm isotropic resolution (*32*). Cells grown on glass surface were cryo-fixed by

high pressure freezing followed by freeze-substitution with osmium tetroxide and uranyl acetate, before resin-embedding. This procedure ensures the best possible structural preservation and enhances the contrast of membranes as well as nucleoproteins (*33*, *34*). Assessment of FIB-SEM of HeLa (G1 and G2) and U2-OS cell nuclei (Fig. 1E and S3A, B) allows identification of distinct CDs as densely packed aggregates of hundreds of highly contrasted ~10 nm sized dots (likely nucleosomes) typically connected by linker filaments (Fig. 1E, Movie S5). Interestingly, chromatin at the nuclear periphery is seen as an inseparable melt, creating a homogeneous, almost continuous chromatin layer, except for NPC holes (Fig. S3C, D). This striking presence of >100 nm sized higher-order domain features is of notable discordance with previous ChromEMT (*35*) results that show a more dispersed distribution of primarily 5-24 nm filaments by using more standard chemical fixation and sample preparation for transmission EM.

Using a machine learning approach (*36*), we next segmented CDs of aggregated nucleosomes distinct from nucleolar and IC regions (Movie S6, Figs. 1F, columns 1-3 and S3D-F). The remaining sites marked solitary 10-20 nm sized nuclear particles (likely RNA-protein complexes such as RNPs or spliceosomes) within the IC. Projection and convolution with a Gaussian function of chromatin and RNPs segmentation probability maps enabled us to generated a close mimic of 3D-SIM micrographs of DNA/RNA stained cells (Fig. 1F, columns 4-6). Quantitative measurements of CD widths along the nuclear envelop yielded an average extend of ~200 ±60 nm. Throughout the nuclear volume, the bulk of CDs have a dimension of between 200-300 nm (Fig. S3D). Smaller CDs (down to 100 nm) and larger CDs (up to > 500 nm) are also apparent, but less frequent (Movie S5).

We conclude the bulk of nuclear RNA and DNA occupy mutually exclusive volumes. Both, 3D-SIM and FIB-SEM independently identify chromatin as a convoluted, reticular structure composed of chains of sub-micrometer CDs.

CDs colocalize with TAD sequences and follow a curvilinear arrangement

Having established the arrangement of chromatin into spatially confined CDs, we used DNA FISH detection to place the observed 3D chromatin landscape in the context of physiological TADs as defined by Hi-C experiments. To avoid harsh denaturation and disruption of chromatin structures below ~1-Mb-size levels (*37*), we have implemented a non-denaturing FISH method, termed resolution after single-stranded exonuclease resection (RASER)-FISH (*38*, *39*). We applied RASER-FISH to study the topology of a previously characterized 0.7 Mb TAD 'H' located on the mouse X chromosome (*15*) (Fig. 2A and S4A). Quantitative analysis of 21 TAD H RASER-FISH signals revealed an average core diameter of ~330 nm (Fig. S4B). Although TADs in single cells are mostly globular they are not uniform and some extend in at least one dimension to a maximum of ~500 nm (Fig. S4B). Importantly, the spatial boundary, or rim of TAD FISH signals coincides with the rim of underlying CDs (Fig. 2A, B). Furthermore, multi-color RASER-FISH of neighboring genomic domains spanning the *α-globin* locus revealed CDs arranged in a curvilinear path (Fig. 2C). Each genomic segment forms a discrete 3D nanodomain along a convoluted chain irrespective of their relative transcriptional activity (Fig. S4C).

We conclude that chromatin in somatic interphase cells arranges as a convoluted curvilinear chain partitioned into discrete non-rigid shaped (globular or extended) CDs. These can harbor TADs and are separated from a DNA-depleted, RNA-occupied interchromatin compartment.

Functional marker distribution reveals 3D zonation at CD scales

The functional output of DNA is influenced by a broad repertoire of protein markers such as histone modifications, architectural proteins, transcription, replication, and chromatin remodeling enzymes. In order to understand how key functional markers mapped against the nuclear landscape at the nanoscale we have devised a pipeline for automated high-content image analysis for the mining of spatial information from thousands of multicolor-labelled 3D-SIM nuclear volume datasets (for details see Fig. S5 and Methods). It first divides the chromatin signal into seven classes based on voxel intensity (*28*), which serve as a proxy for positioning other stainings relative to CD features (Figs. 3A and S5E). The lowest intensity region, class 1 denotes the DNA depleted IC, classes 2 and 3 denote the outer rim or surfaces of CDs, previously termed perichromatin (PC) (*40*), and classes 4-7 constitute the more interior core region of the CDs, with classes 6 and 7 denoting primarily constitutive heterochromatin regions. We characterized the 3D epigenome topography using a wide range of markers (16 in total) associated with specific genome functions (nascent RNA, RNA-associated proteins, chromatin-associated proteins and histone post-translational modifications (PTMs; Figs. 3B and S6A) in over 400 mouse C127 cells in cell cycle stage G1 (Table S1).

The RNA processing/interacting factors hnRNPC1/2, SAF-A (hnRNPU), RNAPII-S2P (marking actively elongating RNAPII) and nascent RNA transcripts are noted as enriched in class 1 (the IC) and the perichromatin classes 2 and 3, depleted in classes 4 and 5, and are virtually absent in the highest classes 6 and 7 (Fig. 3B, top left). A recent study has shown the same pattern to be true for SC35, a protein involved in transcriptional splicing speckles (*41*). Interestingly, those factors known to interact with chromatin, RNAPII-S2P, nascent RNA and SAF-A, show a peak of enrichment in class 2, while the sole factor that only binds RNA, hnRNPC1/2, shows the strongest enrichment in class 1. Accordingly, average nearest-distance measurements to segmented chromatin surface result in a mean distance location of hnRNPC1/2 outside, while the other three markers center right at the border-line (Fig. 3B, top right). These results are in accordance with early immuno-EM observations that active transcription is confined to the PC (*40*). They are also in line with the reported interaction of SAF-A with chromatin-associated RNAs (*42*) supporting the concept of a physical 3D interface between an RNA environment and de-condensed outer CD fringes (Fig. 1B).

Unlike RNA-interacting proteins, the spatial distribution of segmented histone PTMs, which are inherently chromatin-associated, show a marked depletion in the lowest intensity class 1, further validating such annotated voxels as a true interchromatin compartment (IC). Importantly, we observe a biased enrichment for both H3K4me3, typically located at promoters of active genes, and H3K36me3, typically enriched along the body of transcribed genes (Fig. 3B, center left), in the lowest chromatin classes 2 and 3 marking the PC, with peak enrichment in class 2 similar to RNAPII-S2P and nascent transcripts. These markers are rarely found in the higher intensity classes 4 and 5, typically associated with the core of CDs, and are almost absent in the classes 6 and 7 (Fig. 3B, center left). Their corresponding di-methylated forms (H3K4me2 and H3K36me2), as well as acetylated H4K5, which has been implicated in epigenetic bookmarking (*43*) also show a notable albeit less distinct enrichment in the lower class range (peak in class 3) and depletion in higher classes.

In contrast, repressive histone PTMs generally show a broader distribution that is shifted towards the higher intensity classes (Fig. 3B, bottom). The H3K27me3 mark, which is

typically deposited along Polycomb-mediated silenced genes (*44*) shows an enrichment in the interior classes (peaking at class 4). H3K9me3, a marker for transcriptionally inactive facultative and constitutive heterochromatin (*44*), is found enriched towards the CD interior and in heterochromatin classes (3-7), but is most abundant in the higher classes with a peak at class 6. H4K20me3, which has been implicated in silencing repetitive DNA (e.g. in chromocenters of mouse cells) and transposons (*45*), is most strongly enriched in classes 6 and 7, confirming these classes as constitutive heterochromatin. H3K9me2 shows a notably less shifted distribution than H3K9me3 peaking at the interior classes class 4 similarly to H3K27me3.

The observed differential enrichment of functional markers can also be considered in light of the specific enzyme complexes responsible for their deposition. Indeed, there is a remarkable inverse correlation, with smaller complex sizes correlating to peak enrichment in higher chromatin classes of the corresponding marker (Fig. 3C).This supports the hypothesis that chromatin density acts as a higher-level regulator of genome function by hindering physical accessibility of larger complexes to substrate chromatin (*23*). Analyzing a subset of markers in human colon (HCT116) and cervical (HeLa) cancer cell lines in G1 stage, we found highly similar differential spatial distributions, confirming the universal nature of the observed zonation (Fig. S6B, C).

It has been postulated that TADs may be wholly accessible or inaccessible depending on whether they form part of the A or B compartment respectively, as denoted by Hi-C experiments. To test this, we sub-divided the nuclear volume into lamina-associated chromatin plus chromocenter regions, or the residual nuclear volume, as proxies for general B and A compartmentalization, respectively. We find the nanoscale zonation true for both euchromatic ('A') regions as well as heterochromatic ('B') regions (Figs. 3D and S6D).Thus, both large-scale compartments harbor transcriptionally active and inactive sequences with nanoscale distributions, albeit at different ratios (*2*) (Fig. S6E).

In conclusion, our high-content 3D super-resolution mapping approach highlights an ordered zonation of epigenetic markers, forming a nanoscale functional chromatin topography. The propensity of different functions (e.g., transcription silencing) to occupy different chromatin classes is independent of whether that chromatin is found in euchromatic or heterochromatic regions. Markers of active transcription and architectural proteins are confined to the PC (and CD linker regions), while silencing modifications are enriched towards the CD interior. The IC harbors most RNAs and RNA interacting proteins. Finally, we suggest the packing of nucleosomes into mesoscale CDs may lead to the physical exclusion (or hindrance) of chromatin-associated complexes according to their size, thus providing a possible explanation for the ordered functional zonation as a consequence of physical accessibility (*23*).

The local CD topography is temporarily relaxed during DNA replication

DNA polymerase is a large complex and is known to begin replication in a characteristic nuclear pattern of replication foci (*46*). Such observations are in agreement with our finding of larger complexes being enriched at lower chromatin classes. However, DNA replication must eventually process the entire genome, irrespective of the activity state at any given locus. We hypothesize that every chromatin locus should, over time, be locally de-compacted in the process of replication. To test this at the nanometer scale, we identified S-phase cells by short EdU pulse labelling and grouped them into early, mid and late S-phase

stages. Sub-dividing the nucleus in this manner reveals a strong local de-compaction at sites of ongoing replication as revealed by chromatin classification in the local vicinity of EdU foci (Fig. 4A). The disruption is confined to the local activity of the replication machinery, consistent with previous evidence (*21*), as no significant changes could be seen when analyzing the entire nuclear volume (Fig. S7A). Local de-compaction is dramatically highlighted by tunnel-like voids becoming apparent in otherwise dense chromocenters in late S-phase (Fig. 4A, right). This is in agreement with a recent study of DNA synthesis at constitutive heterochromatin (*47*). Accordingly, EdU labelled replication foci show an enrichment in the lower chromatin classes, irrespective of S-phase stage (Fig. 4B).

When quantifying chromatin classes in replicating sub-regions, we observed, as expected, a shift towards denser chromatin classes when progressing from early, to mid, to late S-phase (Fig. 4C). Accordingly, the highest abundance of the active histone PTM H3K4me3 is in early S phase, as compared to the repressive PTM H3K27me3, which is most enriched in mid S phase (Figs. 4D and S7B). Constitutive heterochromatin marks, in particular H4K20me3 become less enriched in denser chromatin classes during late S-phase (Figs. 4 E and S7B) with the replication-driven opening of otherwise condensed chromatin.

Our data shows that active DNA replication can locally disrupt the physical organization of chromatin and consequently its functional zonation.

Cohesin function is dispensable for 3D chromatin structure and functional zonation

While DNA polymerase is able to cause local rearrangements in S phase, other proteins are known to regulate chromatin structure globally throughout interphase. The cohesin complex is able to delineate the genomic boundaries of TADs (*13*) by a loop extrusion mechanism towards convergent CTCF binding sites (*48*). In our analysis, the distributions of CTCF and two sub-units of the cohesin complex, Smc3 and Rad21, were characterized by distinct enrichment in classes 1-2 and depletion in all higher classes (Fig. 3B, left). They also showed a distance profile centering at the 3D-segmented CD chain-IC interface (Fig. 3B, right). Cohesin degradation can erase TADs in Hi-C maps (*14*), but does not erase globular domains in FISH images (*18*). To address the role of cohesin on the global chromatin organization and the spatial zonation of the epigenome, we performed our analyses in human HCT116 cells with an auxin-inducible protease degradation system to ablate the RAD21 subunit of the cohesin complex (*49*) (Fig. 5). In addition, we added a C-terminal HaloTag allowing labeling with variable ligands to monitor the RAD21 expression level in each individual cell (Fig. S8A). Upon addition of both doxycycline and auxin, RAD21 can be depleted with a half-life of 17 min (*49*) and completely ablated in 2 h (Fig. S8B). We hypothesized that if the epigenomic zonation were governed by sequence-specific CTCF-guided cohesin activity, the 3D epigenome should be disrupted, while if this zonation were governed by non-sequence specific biophysical constraints it should not change after cohesin depletion. Strikingly we see no changes in the distribution of representative histone PTMs after 6 h of cohesin depletion (Figs. 5A, B and S8C).

Furthermore, quantitative analysis of HCT116 RAD21-mAID cells 6 h after induction does not show any observable change in the CD chain structure (Fig. 5C-E), nor are there changes in the number of functional histone PTMs on this landscape (Fig. 5F). The CD chain diameter and the ratio of segmented chromatin surface area relative to its volume does not change in the absence of cohesin, suggesting that cohesin is dispensable for these

structures. This phenomenon has recently been observed to persist over longer periods of depletion (*41*).

Our findings demonstrate that loss of cohesin, and thereby of TADs (as defined by Hi-C), has neither an observable effect on maintaining CD structures, nor on the epigenomic zonation relative to CDs in single somatic cells. We conclude that spatial functional zonation is regulated by the physics of the system independent of cohesin function, and therefore not defined by specific sequences with cognate protein complex binding.

DISCUSSION

By applying a rigorous quantitative high-content super-resolution 3D mapping approach of a wide range of functional markers, complemented by FIB-SEM, we establish that chromatin in somatic cells arranges in curvilinear chains of CDs of ~200-300 nm diameter, forming physical modules that subdivide the mammalian genome into functional volumes (Fig. 6A). CDs can harbor individual TADs in single cells and are spatially juxtaposed to and mutually excluded from an RNA-rich interchromatin compartment (IC). The CD chain-IC organization features enrichment of diverse genome functions in different volumes, at the nanometer scale. Active transcription and architectural proteins are confined to the CD chain-IC interface and silencing marks are enriched towards the core of the nucleosomal aggregates (Fig. 6B).

CDs provide an axis of control over DNA-protein interactions

We demonstrate for the first time that nanoscale zonation occurs in both euchromatic and heterochromatic compartments of the nucleus, deviating from previous models of wholly active ‘open’ vs inactive ‘closed’ domains. Based on our data, we postulate that genome segments rich in active sites display a topology of multiple smaller or extended volumes and a higher surface area. Segments depleted in active sites, in contrast, form fewer more globular CDs or melts along the nuclear/nucleolar periphery with reduced surface areas (Fig. 6B, left). The large fraction of non-coding DNA present in the genome despite the associated energetic costs in its accumulation and replication has always been puzzling. However, the potential of CDs to use excess DNA in nucleosome aggregates as regulation by means of accessibility may illuminate a *raison d'être* for much of the genome’s non-coding DNA.

CDs positioned at the nuclear envelope have less active interface due to the lamina blocking one flank. Observations from FIB-SEM reveal that CDs associated with the lamina, that are likely equivalent to lamina associated domains (LADs) (*50*), also lack inter-CD separation by single nucleosome linkers (a feature of CDs in the nuclear interior). Instead, they are form a contiguous melt underneath the nuclear lamina. This conformation further reduces the available surface to just the nucleoplasmic flank (with the exception of channels reaching NPCs). Our model predicts this to favor silencing, which is true for LADs.

The described macro-scale organization can be spatially inverted while maintaining normal physiological function in the nuclei of nocturnal mammalian retina cells (*51*). A model where regulation occurs at the nanometer scale is independent of the nuclear position of the CD at scales of tens of microns, as long as the local CD surface to volume ratio can be controlled. This provides a mechanism for how tissue-specific transcriptional programs can

be established despite large variation in the spatial arrangements of macro compartments between single cells (*52*), even in totally inverted architectures.

The ratio of active CD chain-IC interface area to CD chain volume should regulate genome activity by controlling the accessibility of nuclear machineries to their substrate, chromatin, although it is possible for some (e.g. DNA polymerase, Fig. 6B, right) to overcome these restrictions, reshaping the CD chain. We observe that zonation correlates with the size of chromatin-associated complexes, supporting *in silico* models. In previous modelling, accessibility of transcription factors (TF) is directly correlated to their molecular dimension, suggesting that binding of large TF complexes may 'float as buoys' at domain surfaces, whereas smaller TFs are less affected by the steric hindrance of dense chromatin (*23*).

CDs provide an axis of control over DNA-DNA interactions

We show cohesin activity, while essential for TADs in ensemble Hi-C, to be dispensable for maintaining an interphase chain of consecutive CD. This is in line with a recent study by Bintu et al. demonstrating that local 3D domains can form *de novo* in the absence of cohesin, i.e. in a sequence-unspecific manner (*18*). Interestingly, elevated dynamics of nucleosomes was previously reported upon RAD21 depletion in HeLa cells by single particle tracking (*21*), which hints at more subtle effects on molecular interaction level. At the mesoscale level we conclude that CDs are not TADs, in that CDs represent the naive physical manifestation of chromatin derived primarily from its inherent polymer properties. As such, CD formation is independent of sequence specificity, and so cohesin-independent.

We postulate that the role of cohesin-CTCF is to add a layer of sequence-specificity on top of CDs exploiting the biophysically emergent structures to achieve physiologically relevant regulation between long-range *cis* elements (Fig. 6C, left). Without this cohesin-CTCF bridge between biology and physics two outcomes become apparent. CDs would be composed of non-physiologically relevant sequences, leading to an aberrant transcriptome (Fig. 6C, right). CD composition would also be highly variable from cell to cell leading to an erasure of TAD signal from ensemble population Hi-C.

In contrast to cohesin, we have demonstrated that CDs and their nanoscale zonation can be locally and temporarily disrupted by active replication. The local relaxation of otherwise stable nucleosome aggregates may provide a window of opportunity for gene re-activation or for access by repair machineries to fix DNA damage from replication stress. In such scenarios the ATP-driven activity of cohesin as a loop extruder or as a sister-chromatid clamp may become critical, such as by stabilizing transient local higher-order chromatin structures that increase the fidelity of DNA double strand repair (*39*).

Possible mechanisms of CD formation

The concept of an IC compartment permeating chromosome territories was introduced almost two decades ago (*4*). In such a model, the IC is a channel network that serves as transport highways for macromolecules to and from the nuclear pores. It was postulated that the PR together with the IC constitute the active nuclear compartment (*28*, *53*). Here by high-content analysis from 3D-SIM complemented by FIB-SEM, we show the IC to be a larger volume where a reticular network of CDs is found (Fig. S5B, C). Furthermore, transcriptional activity is enriched at a narrow CD chain-IC interface of < 60 nm in width (Fig. 3B). Most of the IC volume is therefore not involved in active transcription.

Co-staining for bulk RNA and DNA shows clear spatial exclusion of CDs from RNA-filled volumes. In fact, RNA transcripts, of which the vast majority are non-coding (*54*), are typically bound by intrinsically disordered proteins exerting multivalent interactions, known to have phase separating properties (*55*), and many transcription factors are known to have intrinsically disordered domains facilitating phase separation (*56*). It is thus very likely that phase separation contributes to the observed CD architecture by establishing a separation of RNA/protein micro-compartments, away from DNA-rich volumes.

Another driver of CD chain organization could be the default tendency of nucleosomes to self-interact into ever-larger collapsed polymer aggregates ('melts') (*21*). Chromatin domains with coherent dynamics have been reported in recent live-cell and correlated super-resolution imaging of replication domains (*57*). In support of these observations, our FIB-SEM shows CDs as clearly separated entities, many of which are tethered to each other via apparent single nucleosome wide linker filaments (Fig. 1E, cyan arrowheads). These small linkers may offer mechanical coupling along the chain of CDs but remain flexible enough that each CD may move locally and independently from its neighbor. Being accessible, they also offer a site for the start of replication and transcriptional initiation.

These linkers also suggest that 'stabilizing' forces making CDs are counteracted by other forces. If this were not the case, both phase separation or polymer melts would eventually lead to a complete separation of chromatin into a single large unit. We have shown that chromatin destabilization can result from replication in S phase. The destabilization by DNA polymerase may provide a window for transcription factors to access previously inaccessible genes (Fig. 6B, right). We suggest that transcription and co-transcriptional processes supported by repulsive electrostatic forces (exerted by acetylated histone tails) are likewise involved in interphase (e.g.: at linker sites), tipping the local balance towards destabilization.

In conclusion, our novel nano-scale zonation model at the size of single physical CD entities allows for two independent axes of control. The first axis regulates DNA-RNA and DNA-protein interactions (Fig. 6B), the second regulates DNA-DNA *cis* contacts (Fig. 6C). In the first axis, the control of genome function can be achieved through changes in the CD chain surface area. The shape of CDs varies the quantity of chromatin available as substrate to epigenetic remodeler and transcription complexes at the CD-IC interphase. We show this to be true in euchromatic 'A' and heterochromatic 'B' compartments. In the second axis, CDs provide a structure that can be exploited by cohesin-based sequence-specific mechanisms for regulating interaction frequencies between long-range *cis* elements.

Based on these axes, our model predicts smaller domains with a larger surface-to-volume-ratio in constantly replicating pluripotent stem cells, and larger domains with a much-reduced surface-to-volume ratio in terminally differentiated or senescent cells that stop dividing. This would ensure either genome plasticity, or structural 'lock-in' and stabilization of specific functional states, respectively. Specific DNA-protein interactions could be tested in defined subsets of CDs by immunofluorescence relative to single-TAD RASER-FISH. Regulation of DNA-DNA interactions dependent on CD activity states could be monitored by live-cell tracking of multiple *cis* loci within or between individual CDs.

MATERIAL AND METHODS

Plasmids

pSpCas9(BB)−2A-Puro V2.0 targeting RAD21 (PX459 RAD21 (Hs) was described previously (*58*). A poly Glycine-Serine linker, Blasticidin resistance gene (BSD), GSG-P2A, mini auxin-inducible degron (mAID) and HaloTag were cloned between the KpnI and SalI site of a pUC19 vector by Gibson Assembly (NEB #cat E2611). The pUC19 CT-BSD_GSG_P2A-mAID-HaloTag was cloned between two 1 kb homology arms at the 3' of RAD21 to generate pUC19 RAD21 CT-BSD-GSG-P2A-mAID-HaloTag.

BACs

The BACs used for FISH labelling of a single TAD were a gift from E. Heard (*15*). They correspond to X chromosome 'TAD H' characterized between genomic loci 102325818 and 102998976 (673158 bp). The four BACs required to cover this region are: 6-RP24-217I10 (102302874:102459532), 7-RP23-469A2 (102465652:102651023), 8-RP23-331L13 (102648562:102834423) and 9-RP24-396M14 (102804354:102976347) spanning a total length of 673473 bp. The 315bp difference between BACs coverage and TAD boundary calling is considered negligible over the 673kb total (<0.05% error). BAC probes were directly labelled by nick translation using CF-594 (Biotium).

Cell culture

Mouse mammary gland C127 and human cervical cancer HeLa H2B-GFP cells were grown in Dulbecco's Modified Eagle Medium (DMEM) supplemented with 10% FBS, 1% penicillin and streptomycin. Human colon carcinoma HCT116 Tet-OsTIR1 cells were cultivated in McCoy's 5A medium supplemented with 10% FBS, 2 mM L glutamine and 1% penicillin and streptomycin. Human lung fibroblast IMR-90 cells were grown in Dulbecco's Modified Eagle Medium (DMEM) supplemented with 10% FBS, 1% penicillin and streptomycin. Cells were incubated at 37°C, 5% CO2 in a humidified incubator. At 90% confluence cells were trypsinized with 0.05-0.25% Trypsin in PBS or 1x trypsin replacement solution (TrypLE express, Gibco) and passaged to a new culture dish at appropriate dilutions (1:5-1:12 every 2-3 days).

Generation of inducible RAD21 degradation system

To generate a stable HCT116 Tet-OsTIR1 RAD21-mAID-Halo cell line, the pX459 RAD21 (Hs) plasmid and pUC19 RAD21 CT-BSD-GSG-P2A-mAID-HaloTag were transfected using FuGene HD (Promega #cat PRE2311). The sgRNA sequence used to generate the RAD21-mAID-Halo line was: 5'-CCAAGGTTCCATATTATATA-3'. Two days post transfection, cells were grown in blasticidin-containing McCoy's 5A medium (5 μg/mL). After 10 days, single colonies were transferred to 96-well plates and homozygous clones were screened by PCR using the following primers: B2A-BSD: Fw 5'-GCTCCTATTAGCCCTCCCACACATAACC-3', Rev 5'-GGATGTATAAAGGTTCCGGAGCCACCAAC-3'; RAD21 (fragment 3): Fw 5'- AGGG CTAATAAGGAGCTAGAAGCATTATAGC -3', Rev 5'- TTGCATGCCTGCAGGGTTCCAAAC CAGGAGTGTG -3'; RAD21 (fragment 1): Fw 5'- AATTCGAGCTCGGTACTGAATGTCTGCA AAATGCCAAGC -3', Rev 5'- CTTCTCCTTGCCGGAAATCTCGAGCGTC -3'; mAID: Fw 5'-TTTCCGGCAAGGAGAAGAGTGCTTGTC-3', Rev 5'- CCGGAACCTTTATACATCCTCAAT

CGATTTTC-3'; Genomic primer: Fw 5'- AGCATGAGATTGGAGGGGA-3', Rev 5'- GCCACT CAACATTATTACATGCA-3'.

EdU, EU and BrUTP labelling and perturbation experiments

To identify cells in S-phase 10 μM 5-ethynyl-deoxyuridine (EdU) was added 15-30 min before fixation. G1 cells were identified by being negative for EdU pulse labelling and having a smaller nuclear size compared to G2 cells. For bulk RNA labelling 1 mM 5-ethynyluridine (EU) was added 60-90 min before fixation. To label nascent RNA, a 10 min BrUTP pulse labelling was performed by a scratch transcription labelling approach as previously described (*59*). For auxin-induced RAD21-degradation, HCT116 cells were cultured in the presence of 5 μg/mL doxycycline (Sigma, D9891) and 500 μM auxin (Sigma, cat# I5148) for 16 h and 6 h, respectively.

RASER-FISH and probe labelling

RASER-FISH maintains nuclear fine-scale structure by replacing heat denaturation with Exonuclease III digestion of one of the two DNA strands after UV-induced generation of nicks, and is suitable for high- and super-resolution imaging analysis (*38*). Briefly, cells were labelled overnight with a BrdU/BrdC mix (3:1) at a final concentration of 10 μM. Cells were fixed in 2% formaldehyde for 15 min and permeabilized in 0.2% Triton X-100/PBS (vol./vol.) for 10 min. Cells were incubated with 4',6-diamidino-2-phenylindole (DAPI; 0.5 μg/mL in PBS), exposed to 254 nm wavelength UV light for 15 min, then treated with Exonuclease III (NEB) at a final concentration of 5 U/μL at 37°C for 15 min. Labelled probes (100 ng each) were denatured in hybridization mix at 90°C for 5 min and pre-annealed at 37°C for 20 min. Coverslips were hybridized with prepared probes at 42°C.

Immunofluorescence (IF) labelling

IF labelling was performed as described in detail (*60*, *61*). The antibodies used in this investigation are listed in Table S2. One day before labelling, cells were grown on 22x22 mm #1.5H high precision 170 µm ± 5 µm coverslips (Marienfeld Superior). HCT116 Tet-OsTIR1 RAD21-mAID-Halo cells were fluorescently tagged by incubating with 50 nM diAcFAM HaloTag ligand (Promega, cat# G8272) or 500 nM JF646 HaloTag ligand (gift from L. Lavis) for 30 min to monitor the expression level of individual cells. HCT116 cells were incubated in HaloTag-free medium for 30 min to remove residual ligand. Prior to fixation, cells were washed twice with PBS. Cells were fixed in 2% formaldehyde/PBS (Sigma, #cat F8775) for 10 min, washed with 0.02% Tween-20/PBS (PBST) and permeabilized in 0.1-0.5% Triton-X-100/PBS. Coverslips were washed three times with PBST and incubated for 30 min in MaxBlock (Active Motif, cat# 15252). Cells were stained with primary antibodies against the protein of interest, washed three times with PBST and stained with fluorescently-labelled secondary antibodies. After washing, cells were post-fixed in 4% formaldehyde/PBS for 10 min and counterstained using 1-2 μg/mL DAPI or 1 μM SYTOX Green for 10 min. DAPI has a bias towards adenine and thymine over guanine and cytosine making AT-enriched satellite repeats near centromeric constitutive heterochromatin more intensively stained. This is particularly prominent in the chromocenters of mouse cells. This non-linear correlation between signal intensity and DNA concentration meant DAPI was replaced by SYTOX for all experiments possible. SYTOX has a weak affinity to bind RNA at high concentrations. Incubation with 1–10 U RNAse I/PBS prior to SYTOX counterstaining was

performed as described (*59*). Coverslips were mounted in non-hardening Vectashield (Vector Laboratories, cat# H-1000) and stored at 4°C.

Super-resolution image acquisition, reconstruction and quality control

3D-SIM images were acquired with a DeltaVision OMX V3 Blaze system (GE Healthcare) equipped with a 60x/1.42 NA PlanApo oil immersion objective (Olympus), pco.edge 5.5 sCMOS cameras (PCO) and 405, 488, 593 and 640 nm lasers. For fixed cell imaging, 3D image stacks were acquired over the whole cell volume in z and with 15 raw images per plane (five phases, three angles). Spherical aberration was minimized using immersion oil with RI 1.514 for sample acquisition. The raw data was computationally reconstructed with SoftWoRx 6.5.2 (GE Healthcare) using channel-specific OTFs recorded using immersion oil with RI 1.512, and Wiener filter settings between 0.002-0.006 to generate 3D stacks of wavelength-dependent 110-130 nm lateral and ~320 nm axial resolution. Due to its broad emission spectrum 405 nm excited DAPI staining was typically detected in the green emission range (and reconstructed with the 'green' OTF) as this empirically improved the reconstruction quality. The system's resolution was confirmed by measurements of monolayers of 100 nm diameter yellow-green and red FluoSpheres (Thermo Fisher) (*61*). All SIM data was routinely and meticulously quality controlled for effective resolution and absence of artifacts using SIMcheck (*62*), an open-source Image J plugin to assess SIM image quality via modulation contrast-to-noise ratio, spherical aberration mismatch, reconstructed Fourier plot and reconstructed intensity histogram values (*61*). Multi-channel acquisitions were aligned in 3D using Chromagnon software (*63*) based 3D-SIM acquisitions of multicolor EdU labelled C127 cells (*60*). 3D-SIM imaging of DAPI or SYTOX Green stained DNA typically provides a highly-contrasted spatial representation of chromatin distribution with a lateral resolution of ~110 nm in lateral and ~320 nm in axial direction (Fig. S1A).

For live cell 3D-SIM, HeLa H2B-GFP cells were seeded in a 35 mm μ-Dish, high Glass Bottom (Ibidi) using phenol red-free DMEM medium supplemented with 10 μM HEPES. Live cell imaging was performed at 37°C and 5% CO_2 supply by using an objective heater and a stage top incubator. To improve the temporal resolution and reduce bleaching, only a central nuclear sub-region of 7 z-positions with 125 nm interval was recorded (minimum required for 3D reconstruction), covering a total range of 0.75 μm and totaling 105 raw images (5 phases x 3 angles x 7 z-positions) per timepoint. Using a 10 ms exposure time, frame rates of down to 0.5 Hz could be achieved, and typically 12 to 18 time points could be recorded until the photon budget was exhausted due to photobleaching, with high frequency noise ('hammer finish') artifacts becoming overly prominent (*61*). The reconstructed z-sections were processed in FIJI applying a maximum intensity z-projection followed by Bleach Correction (histogram matching) and Linear Stack Alignment with SWIFT (affine transformation) to compensate for photobleaching and nuclear motion/deformation. Confining to a minimal stack height and subsequent projection further minimizes 'z-wrapping' artifacts described in ref. (*61*). It is important to note, that the above described measures to enable live cell 3D-SIM come at the expense of extended focus depth with reduced axial resolution (Fig. S1C), and degrading reconstruction quality over time (Movies S1-S3).

Quality validation

3D-SIM imaging and subsequent quantitative analyses is susceptible to artefacts (*61*). For instance, bulk labelling of densely packed chromatin inside mammalian nuclei of several μm depth entails high levels of out-of-focus blur, which reduces the contrast of illumination stripe modulation and thus the ability to recover high frequency (i.e., super-resolution) structural information. We therefore carefully assessed and optimized system performance as well as raw and reconstructed data quality using the SIMcheck ImageJ plugin (*62*) (Fig. S1A). To exclude potential false positive calls of nuclear marker signals, we used the modulation contrast-to-noise ratio (MCNR) map function of SIMcheck, which generates a metric of local stripe contrast in different regions of the raw data and directly correlates this with the level of high-frequency information content in the reconstructed data (*61*). Only immunofluorescent spot signals whose underlying MCNR values exceed a stringent quality threshold were considered while localizations with low underlying MCNR values were discarded to exclude any SIM signal which falls below reconstruction confidence. This criterion was applied to all datasets before feeding these to the analysis pipeline (Fig. S9). We noted that most nuclear spots (between a few hundred to several thousand per nucleus, depending on the target and the antibody) were in the size range of a 3D-SIM resolution-limited point signal, and that their intensities were similar to those few extranuclear spots originating from non-specifically bound primary-secondary antibody complexes containing fewer than 10 dye molecules. We therefore conclude that nuclear signals predominantly represent the binding of a primary-secondary antibody complex to a single epitope.

Focused ion beam scanning electron microscopy (FIB-SEM)

Cryo-fixed HeLa (CCL-2) or U2-OS cells were prepared for FIB-SEM as described previously (*34*). Briefly, cells grown on sapphire coverslips (3-mm diameter, 0.05-mm thickness; Nanjing Co-Energy Optical Crystal Co.) were subjected to high-pressure freezing using a Compact 01 high-pressure freezer (Wohlwend), followed by freeze-substitution (FS) under liquid N_2 in FS medium (2% OsO_4, 0.1% uranyl acetate, and 3% water in acetone) using an automated AFS2 machine (Leica Microsystems). Samples were washed immediately after FS three times in anhydrous acetone for a total of 10 min, and embedded in Eponate 12. FIB-SEM imaging was performed using a customized Zeiss Gemini 500 (HeLa) or Zeiss Merlin (U2-OS) crossbeam system previously described (*32*). The Zeiss Capella FIB column was repositioned at a 90° angle to the SEM column. The block face was imaged by a 240 pA electron beam with 1.0 keV landing energy at 200 kHz (HeLa) or by a 2 nA electron beam with 1.2 keV landing energy at 500 kHz (U2-OS). The x-y pixel resolution was set at 4 nm (HeLa) and 8 nm (U2-OS). A focused Ga ion beam of 15 nA at 30 keV milled away ~3 nm (HeLa 'G1'), ~5.6 nm (HeLa 'G2'), and ~5 nm (U2-OS) of material from the block face for each section (thickness estimated based on the average of SEM working distance and FIB milling voltage). The newly exposed surface was then imaged again. The milling / imaging cycle continued about once every 150 s for one month to capture an entire cell (50 x 8 x 68 μm^3) at 4 nm voxel (HeLa) or every 40 s for 6 days to capture an entire cell (104 x 8 x 42 μm^3) at 8 nm voxel (U2-OS). Each raw image stack was aligned and registered using a scale invariant feature transform (SIFT) plug-in through Fiji (*64*), the U2-OS cell volume was further binned by a factor of 2 along the milling axis. A subvolume containing the nucleus was cropped from the whole cell stack for further processing and analysis. To correct for variations in the FIB milling thickness and ensure

isotropic voxel sizes, a rescaling along the milling axis of 75% (HeLa 'G1'), 140% (HeLa 'G2') and 125% (U2-OS) was applied (confirmed by the roundness of outer nuclear pore rings in horizontal planes). Machine learning based segmentation of FIB-SEM data was performed using Ilastik 1.3.3 (*36*). 3D volume rendering after segmentation was performed with Imaris 9.2.

ChaiN – a pipeline for high-content analysis of the 3D epigenome

ChaiN (Chain high-throughput analysis of the *in situ* Nucleome) describes a pipeline of scripts for the automated high-throughput analyses in this investigation (Fig. S5). In brief, the counterstain/chromatin channel is used to generate (1) a nuclear mask and (2) segment chromatin topography into 7 intensity-based classes using an R script that is expanding on a Hidden Markov model (*65*). The modal intensity value (comprised of the large volume outside of the nucleus) is used to calibrate the relative intensity levels of each micrograph (due to unknown DNA dye incorporation and adjusted imaging conditions for optimized SIM imaging). Nucleoli were used as internal controls, as no signal should be detected in these volumes as expected. While this anchors the lower limit of the dynamic range, the upper limit is always relative to the maximum intensity value per micrograph, a limitation of the technique where cells of different conditions cannot be imaged together in the same micrograph for paired analysis. Nevertheless, based on the output of ChaiN, we can quantitatively assess multiple parameters, such as the overall volume of the PC+CD (combined classes 2-7, Fig. S5C) versus the IC (class 1), the PC-IC 3D surface, and the surface-to-volume-ratio. We note that the total number of discrete segmentation bins used in this analysis is arbitrary, with the sole criterion to group all non-detectable chromatin voxels as one class (class 1, IC).

The IF signals are thresholded by intensity using the Otsu algorithm, with all non-foci voxels replaced by zeros. The complement of this image is segmented by a 3D watershed algorithm and the 3D centroid coordinates are extracted from each segmented region's center of mass after weighting by local pixel intensities. To filter out potential false positive localizations, a local modulation-contrast-to-noise-ratio (MCNR) threshold is used to avoid potential artefacts skewing the statistical output (*61*, *62*). An MCNR-mask was generated (using quality cut-off at: MCN=5). Thresholded images together with the MCNR-mask were used as input for ChaiN to discard sub-quality voxels in the marker signal foci, reducing the effect of 3D-SIM artefacts on subsequent image analysis.

For each marker and condition at least 20 3D datasets from 2 biological replicates were acquired, each with many hundreds to several thousands of annotated IF foci. Where relevant, significance testing was performed using a Student's t-test.

The quality controlled and filtered centroid positions were then related to the chromatin-interchromatin volume in two ways: (1) The spot positions falling into each of the 7 segmented classes were counted, normalized to the respective class size, and their relative enrichment (or depletion) displayed in a heat map on a log 2-fold scale. Indexing IF coordinates on the segmented chromatin yields their enrichment or depletion profiles at different chromatin densities normalized to the volumes of each chromatin class.
(2) Segmentation of the 3D surface between class 1 and all other classes allows for a Euclidian distance calculation between the IF coordinates and the nearest CD chain surface voxel.

Quantitative evaluation of chromatin dynamics

Spatial correlation dynamics of chromatin was estimated by using Dense Flow reConstruction and Correlation (DFCC) (*29*). Briefly, DFCC was applied to estimate the 2D apparent motion of two consecutive images in an image sequence (N-1); the direction and magnitude of flow fields of each pixel (size = 41 nm) were estimated for H2B-GFP over a 20-image series and with a time interval of 2 s. Then, spatial auto-correlation of scalar fields representing motion direction was calculated by Fast Fourier Transforms given by

$$r(\Delta x, \Delta y) = \frac{\mathcal{F}^{-1}[\mathcal{F}(\gamma) \cdot \mathcal{F}^{*}(\gamma)]}{\langle\gamma\rangle\langle\gamma\rangle},$$

where $\mathcal{F}(\cdot)$, $\mathcal{F}^{-1}(\cdot)$, and $\mathcal{F}^{*}(\cdot)$ are the Fourier transformation, inverse Fourier transformation and the complex conjugate of the Fourier transformation, respectively. Correlation was calculated as a function of space lag and fitted using the Whittle-Màtern model:

$$r(\rho) = \frac{2^{1-\nu}}{\Gamma(\nu)}\left(\frac{\rho}{\rho_c}\right)^{\nu} K_{\nu}\left(\frac{\rho}{\rho_c}\right),$$

where, ρ_c and ν are the correlation length and a smoothness parameter, respectively. Correlation length and the smoothness parameter were derived from the regression and shown over the time lag. The parameters were averaged for each time interval over all accessible time points.

The Hi-D method was applied to estimate the biophysical properties of chromatin motion in living Hela cells at single-pixel resolution (41 nm) (*66*). Mean square displacement (MSD) curves were plotted over time lags representing the trajectories of chromatin in the entire nucleus. Then, a Bayesian inference approach was applied to test the following five principle models for each MSD curve in order to classify types of motion. Fitting of the MSD curve derived from trajectories can be expressed for anomalous diffusion (α), free diffusion constant (D), directed motion (V), or a combination thereof. The value of each biophysical parameter extracted by this fitting is then mapped in a 2D color map, and the five principal models are shown as a colored map directly on the nucleus (Fig. S3C). The five possible models for each MSD curve are:

$$MSD_D(\tau) = 4D\tau + o$$
$$MSD_{DA}(\tau) = 4D\tau^{\alpha} + o$$
$$MSD_V(\tau) = v^2\tau^2 + o$$
$$MSD_{DV}(\tau) = 4D\tau + v^2\tau^2 + o$$
$$MSD_{DAV}(\tau) = 4D\tau^{\alpha} + v^2\tau^2 + o$$

where: D is the abbreviation of Free diffusion model; DA is for Anomalous diffusion model; V is for Drift velocity model; DV is for Free diffusion + drift model; DAV is for Anomalous diffusion + drift model; α is anomalous diffusion constant; τ is time interval; o is a constant offset added to every model.

REFERENCES AND NOTES

1. J. H. Gibcus, J. Dekker, The hierarchy of the 3D genome. *Mol. Cell.* **49**, 773–782 (2013).
2. M. J. Rowley, V. G. Corces, Organizational principles of 3D genome architecture. *Nat. Rev. Genet.* **19**, 789–800 (2018).
3. K. Luger, A. W. Mäder, R. K. Richmond, D. F. Sargent, T. J. Richmond, Crystal structure of the nucleosome core particle at 2.8 A resolution. *Nature.* **389**, 251–60 (1997).
4. T. Cremer, C. Cremer, Chromosome territories, nuclear architecture and gene regulation in mammalian cells. *Nat. Rev. Genet.* **2**, 292–301 (2001).
5. C. Adriaens *et al.*, Blank spots on the map: some current questions on nuclear organization and genome architecture. *Histochem. Cell Biol.* **150**, 579–592 (2018).
6. J. R. Dixon *et al.*, Topological domains in mammalian genomes identified by analysis of chromatin interactions. *Nature.* **485**, 376–380 (2012).
7. A. D. Schmitt, M. Hu, B. Ren, Genome-wide mapping and analysis of chromosome architecture. *Nat. Rev. Mol. Cell Biol.* **17**, 743–755 (2016).
8. E. Lieberman-Aiden *et al.*, Comprehensive mapping of long-range interactions reveals folding principles of the human genome. *Science.* **326**, 289–293 (2009).
9. B. van Steensel, A. S. Belmont, Lamina-Associated Domains: Links with Chromosome Architecture, Heterochromatin, and Gene Repression. *Cell.* **169**, 780–791 (2017).
10. J. E. Phillips, V. G. Corces, CTCF: Master weaver of the genome. *Cell.* **137**, 1194–1211 (2009).
11. D. G. Lupiáñez *et al.*, Disruptions of topological chromatin domains cause pathogenic rewiring of gene-enhancer interactions. *Cell.* **161**, 1012–1025 (2015).
12. M. Merkenschlager, E. P. Nora, CTCF and cohesin in genome folding and transcriptional gene regulation. *Annu. Rev. Genomics Hum. Genet.* **17**, 17–43 (2016).
13. S. Yatskevich, J. Rhodes, K. Nasmyth, Organization of Chromosomal DNA by SMC Complexes. *Annu. Rev. Genet.* **53**, 445–482 (2019).
14. S. S. P. Rao *et al.*, Cohesin loss eliminates all loop domains. *Cell.* **171**, 305-320.e24 (2017).
15. E. P. Nora *et al.*, Spatial partitioning of the regulatory landscape of the X-inactivation centre. *Nature.* **485**, 381–385 (2012).
16. T. Nagano *et al.*, Single-cell Hi-C reveals cell-to-cell variability in chromosome structure. *Nature.* **502**, 59–64 (2013).
17. I. M. Flyamer *et al.*, Single-nucleus Hi-C reveals unique chromatin reorganization at oocyte-to-zygote transition. *Nature.* **544**, 110–114 (2017).
18. B. Bintu *et al.*, Super-resolution chromatin tracing reveals domains and cooperative interactions in single cells. *Science.* **362**, eaau1783 (2018).
19. E. H. Finn *et al.*, Heterogeneity and intrinsic variation in spatial genome organization. *Cell.* **176**, 1502–1515 (2019).
20. K. Maeshima *et al.*, Nucleosomal arrays self-assemble into supramolecular globular structures lacking 30-nm fibers. *EMBO J.* **35**, 1115–1132 (2016).
21. T. Nozaki *et al.*, Dynamic organization of chromatin domains revealed by super-resolution live-cell imaging. *Mol. Cell.* **67**, 282-293.e7 (2017).
22. A. N. Boettiger *et al.*, Super-resolution imaging reveals distinct chromatin folding for different epigenetic states. *Nature.* **529**, 418–422 (2016).
23. K. Maeshima *et al.*, The physical size of transcription factors is key to transcriptional regulation in chromatin domains. *J. Phys. Condens. Matter.* **27**, 064116 (2015).
24. Q. Szabo *et al.*, TADs are 3D structural units of higher-order chromosome organization in Drosophila. *Sci. Adv.* **4**, 1–14 (2018).

25. L. Schermelleh *et al.*, Super-resolution microscopy demystified. *Nat. Cell Biol.* **21**, 72–84 (2019).
26. L. Schermelleh *et al.*, Subdiffraction multicolor imaging of the nuclear periphery with 3D structured illumination microscopy. *Science.* **320**, 1332–1336 (2008).
27. Y. Markaki *et al.*, Functional nuclear organization of transcription and DNA replication: A topographical marriage between chromatin domains and the interchromatin compartment. *Cold Spring Harb. Symp. Quant. Biol.* **75**, 475–492 (2010).
28. D. Smeets *et al.*, Three-dimensional super-resolution microscopy of the inactive X chromosome territory reveals a collapse of its active nuclear compartment harboring distinct Xist RNA foci. *Epigenetics Chromatin*. **7**, 8 (2014).
29. H. A. Shaban, R. Barth, K. Bystricky, Formation of correlated chromatin domains at nanoscale dynamic resolution during transcription. *Nucleic Acids Res.* **46**, e77 (2018).
30. R. Bruinsma, A. Y. Grosberg, Y. Rabin, A. Zidovska, Chromatin hydrodynamics. *Biophys. J.* **106**, 1871–1881 (2014).
31. C. Y. Jao, A. Salic, Exploring RNA transcription and turnover in vivo by using click chemistry. *Proc. Natl. Acad. Sci.* **105**, 15779–15784 (2008).
32. C. S. Xu *et al.*, Enhanced FIB-SEM systems for large-volume 3D imaging. *Elife*. **6**, 1–36 (2017).
33. C.-L. Chang *et al.*, Spastin tethers lipid droplets to peroxisomes and directs fatty acid trafficking through ESCRT-III. *J. Cell Biol.* **218**, 2583–2599 (2019).
34. D. P. Hoffman *et al.*, Correlative three-dimensional super-resolution and block-face electron microscopy of whole vitreously frozen cells. *Science.* **367** (2020).
35. H. D. Ou *et al.*, ChromEMT: Visualizing 3D chromatin structure and compaction in interphase and mitotic cells. *Science.* **357**, 1–36 (2017).
36. S. Berg *et al.*, Ilastik: Interactive machine learning for (bio)image analysis. *Nat. Methods*. **16**, 1226–1232 (2019).
37. Y. Markaki *et al.*, The potential of 3D-FISH and super-resolution structured illumination microscopy for studies of 3D nuclear architecture. *BioEssays*. **34**, 412–426 (2012).
38. J. M. Brown *et al.*, A tissue-specific self-interacting chromatin domain forms independently of enhancer-promoter interactions. *Nat. Commun.* **9**, 1–15 (2018).
39. F. Ochs *et al.*, Stabilization of chromatin topology safeguards genome integrity. *Nature*. **574**, 571–574 (2019).
40. S. Fakan, R. van Driel, The perichromatin region: A functional compartment in the nucleus that determines large-scale chromatin folding. *Semin. Cell Dev. Biol.* **18**, 676–681 (2007).
41. M. Cremer *et al.*, Cohesin depleted cells pass through mitosis and reconstitute a functional nuclear architecture. *bioRxiv*. **816611** (2019).
42. R. S. Nozawa *et al.*, SAF-A regulates interphase chromosome structure through oligomerization with chromatin-associated RNAs. *Cell*. **169**, 1214-1227.e18 (2017).
43. R. Zhao, T. Nakamura, Y. Fu, Z. Lazar, D. L. Spector, Gene bookmarking accelerates the kinetics of post-mitotic transcriptional re-activation. *Nat. Cell Biol.* **13**, 1295–1304 (2011).
44. S. Dambacher, M. Hahn, G. Schotta, Epigenetic regulation of development by histone lysine methylation. *Heredity.* **105**, 24–37 (2010).
45. G. Schotta *et al.*, A silencing pathway to induce H3-K9 and H4-K20 trimethylation at constitutive heterochromatin. *Genes Dev.* **18**, 1251–1262 (2004).
46. V. O. Chagin *et al.*, 4D Visualization of replication foci in mammalian cells corresponding to individual replicons. *Nat. Commun.* **7**, 11231 (2016).
47. V. O. Chagin *et al.*, Processive DNA synthesis is associated with localized decompaction of constitutive heterochromatin at the sites of DNA replication and repair. *Nucleus*. **10**, 231–253 (2019).

48. I. F. Davidson *et al.*, DNA loop extrusion by human cohesin. *Science*. **3418**, 1–13 (2019).
49. T. Natsume, T. Kiyomitsu, Y. Saga, M. T. Kanemaki, Rapid protein depletion in human cells by auxin-inducible degron tagging with short homology donors. *Cell Rep.* **15**, 210–218 (2016).
50. J. Kind *et al.*, Single-cell dynamics of genome-nuclear lamina interactions. *Cell*. **153**, 178–192 (2013).
51. I. Solovei *et al.*, Nuclear architecture of rod photoreceptor cells adapts to vision in mammalian evolution. *Cell*. **137**, 356–368 (2009).
52. B. Joffe, H. Leonhardt, I. Solovei, Differentiation and large scale spatial organization of the genome. *Curr. Opin. Genet. Dev.* **20**, 562–569 (2010).
53. T. Cremer *et al.*, The 4D nucleome: Evidence for a dynamic nuclear landscape based on co-aligned active and inactive nuclear compartments. *FEBS Lett.* **589**, 2931–2943 (2015).
54. A. F. Palazzo, E. S. Lee, Non-coding RNA: What is functional and what is junk? *Front. Genet.* **5**, 1–11 (2015).
55. A. I. Järvelin, M. Noerenberg, I. Davis, A. Castello, The new (dis)order in RNA regulation. *Cell Commun. Signal.* **14**, 9 (2016).
56. Y. Shin *et al.*, Liquid nuclear condensates mechanically sense and restructure the genome. *Cell*. **175**, 1481-1491.e13 (2018).
57. W. Xiang *et al.*, Correlative live and super-resolution imaging reveals the dynamic structure of replication domains. *J. Cell Biol.* **217**, 1973–1984 (2018).
58. J. Rhodes, D. Mazza, K. Nasmyth, S. Uphoff, Scc2/Nipbl hops between chromosomal cohesin rings after loading. *Elife*. **6**, 1–20 (2017).
59. E. Miron, C. Innocent, S. Heyde, L. Schermelleh, in *Methods in Molecular Biology: Chromosome Architecture: Methods and Protocols*, M. C. Leake, Ed. (2016), vol. 1431, pp. 127–140.
60. F. Kraus *et al.*, Quantitative 3D structured illumination microscopy of nuclear structures. *Nat. Protoc.* **12**, 1011–1028 (2017).
61. J. Demmerle *et al.*, Strategic and practical guidelines for successful structured illumination microscopy. *Nat. Protoc.* **12**, 988–1010 (2017).
62. G. Ball *et al.*, SIMcheck: A toolbox for successful super-resolution structured illumination microscopy. *Sci. Rep.* **5**, 15915 (2015).
63. A. Matsuda, L. Schermelleh, Y. Hirano, T. Haraguchi, Y. Hiraoka, Accurate and fiducial-marker-free correction for three-dimensional chromatic shift in biological fluorescence microscopy. *Sci. Rep.* **8**, 7583 (2018).
64. J. Schindelin *et al.*, Fiji: an open-source platform for biological-image analysis. *Nat. Methods*. **9**, 676–82 (2012).
65. V. J. Schmid, M. Cremer, T. Cremer, Quantitative analyses of the 3D nuclear landscape recorded with super-resolved fluorescence microscopy. *Methods*. **123**, 33–46 (2017).
66. H. A. Shaban, R. Barth, K. Bystricky, Hi-D: Nanoscale mapping of nuclear dynamics in single living cells. *Genome Biol.* **21**, 1–21 (2020).

Acknowledgments: We thank Edith Heard for providing FISH probes against X-chromosomal TADs, Luke Lavis for providing JF646 HaloTag ligand, Ron Schwessinger for help visualizing the C127 genome tracks, Afaf El-Sagheer and Arun Shivalingam for assistance in oligonucleotide synthesis, Anna Kreshuk and Jakop Pospisil for assistance with Ilastik and Imaris, as well as Phoebe Oldach and Eva Parisi for technical help. We are also indebted to Gleb Shtengel, Amalia Pasolli and Aubrey Weigel for help with FIB-SEM

sample preparation and imaging, and David Brown and Rob Klose for providing H3K4me3 ChIP-Seq and ATAC-Seq data. We further wish to thank all colleagues who proofread and commented on the manuscript, in particular Fena Ochs, Justin Demmerle, Jiri Lukas, Claudia Lukas, Tim Nott and Rob Klose for valuable suggestions. **Funding:** Imaging was performed at the Micron Oxford Advanced Bioimaging Unit funded by a Wellcome Trust Strategic Award (091911 and 107457/Z/15/Z). L.S. further acknowledges support by the John Fell Oxford University Press (OUP) Research Fund 143/064 and by the European Union's Horizon 2020 research and innovation program under the Marie Sklodowska-Curie Grant Agreement No. 766181. A research visit of H.A.S. in the L.S. lab was enabled by an AfOx travel grant of the Africa-Oxford Initiative. E.M. further acknowledges support by the Sydney Perry Foundation & Covenantors Educational Fund. S.d.O. was supported by grants from the BBSRC (BB/L01811X/1) and the MRC (MR/N00969X/1). Research in the V.B. lab is supported by MRC grants MC_UU_00016/1 and MR/N00969X/1, the latter in collaboration with Prof Jim Hughes, WIMM and by BBSRC grant BB/L01811X held in collaboration with Tom Brown (Department of Physical Chemistry, Oxford University) and further supported by the Wolfson Imaging Centre Oxford funded by the Wolfson Foundation, joint MRC/BBSRC/EPSRC and the Wellcome Trust. **Author contributions:** E.M. and L.S. conceived the project and designed the experiments. C.S.X and H.F.H. conceived and conducted cryo-sample preparation and FIB-SEM imaging. E.M., R.O., H.A.S. and D.M.S.P. wrote the software and performed analyses. J.B. and V.B. devised the FISH protocol. E.M., R.O., J.B., A.R.C.F., S.d.O., C.I., J.R. and L.S. carried out experiments. E.M., R.O. and L.S. wrote the manuscript and generated the figures with contributions from all authors. **Competing interests:** Authors declare no competing interests. **Data and code availability:** All data, parameters and scripts used are available for reproducing the results of this investigation. Raw and reconstructed 3D-SIM are available at the Image Data Resource (IDR). The programs required to run all scripts for ChaiN are: ImageJ (FIJI distribution with SIMcheck), R and Octave. The live cell analysis via DFCC and Hi-D are run on Matlab with Image Processing, Signal Processing and Statistics and Machine Learning Toolboxes in a Windows environment. Scripts for ChaiN, DFCC and Hi-D analysis are available in the following GitHub repositories: https://github.com/ezemiron/Chain, https://github.com/romanbarth/DFCC, and https://github.com/romanbarth/Hi-D, respectively.

FIGURES

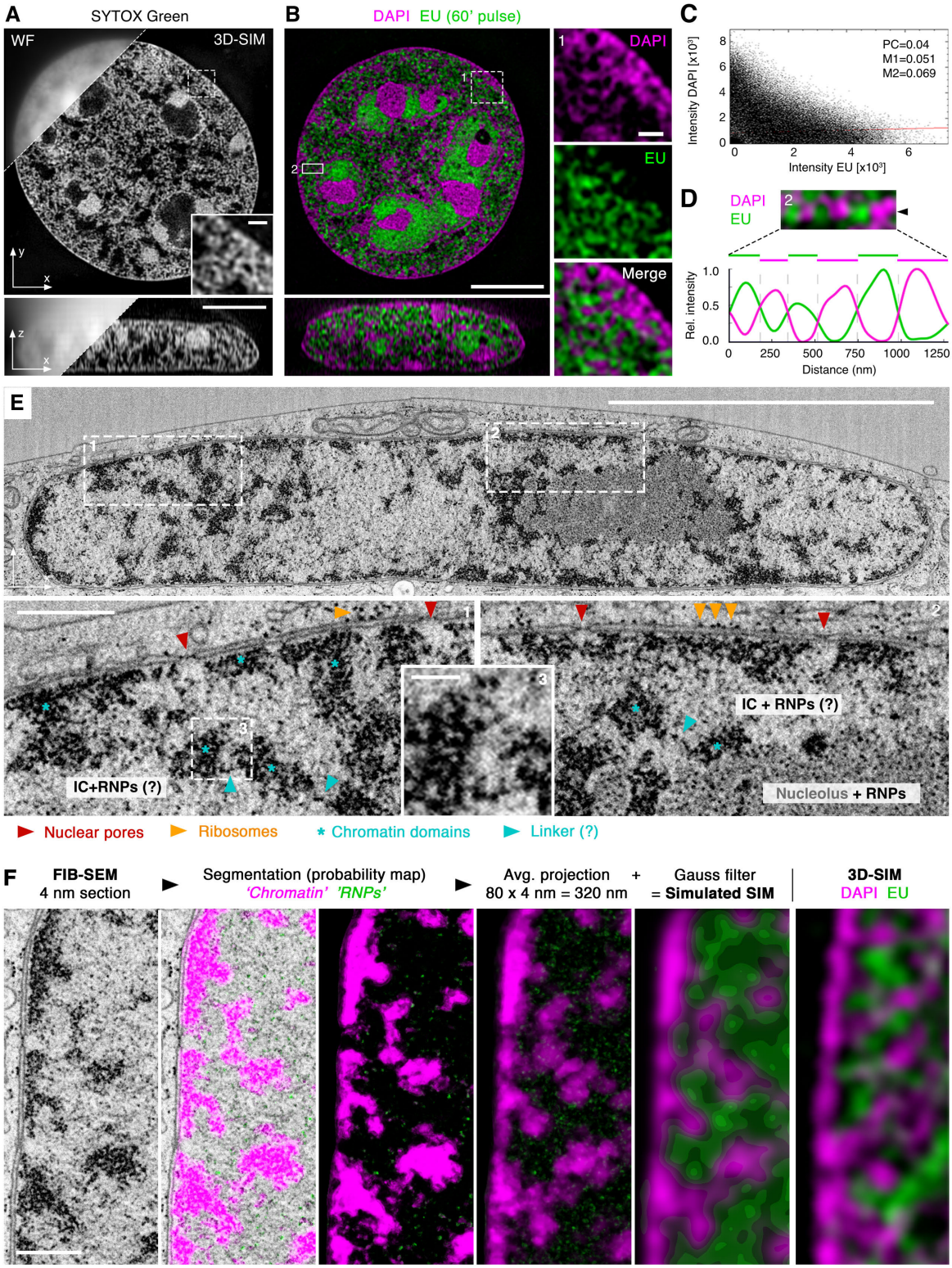
A
SYTOX Green
WF
3D-SIM
B
DAPI EU (60' pulse)
DAPI
EU
Merge
C
PC=0.04
M1=0.051
M2=0.069
Intensity DAPI [x10³]
Intensity EU [x10³]
D
DAPI
EU
Rel. intensity
Distance (nm)
E
IC+RNPs (?)
IC + RNPs (?)
Nucleolus + RNPs
Nuclear pores
Ribosomes
Chromatin domains
Linker (?)
F
FIB-SEM
4 nm section
Segmentation (probability map)
'Chromatin' 'RNPs'
Avg. projection
80 x 4 nm = 320 nm
+
Gauss filter
= Simulated SIM
3D-SIM
DAPI EU

Fig 1. Chromatin folds into 3D nanodomains of nucleosomal aggregates distinct from an RNA-occupied interchromatin network. (**A**) In contrast to conventional widefield (WF, top left), super-resolution 3D-SIM of fixed mouse C127 mammary epithelial cells resolves SYTOX Green stained chromatin as a sponge-like reticular structure throughout the nuclear volume. Chromatin is separated by an unstained interchromatin (IC) space. Top panel shows a lateral, bottom panel an orthogonal cross section through the 3D image stack. Scale bars: 5 μm and 0.5 μm (inset). See also Fig. S1. (**B**) IC juxtaposed to DAPI-stained chromatin is largely occupied by bulk RNAs stained with EU (60 min pulse). Right, inset magnifications of region 1, and below, orthogonal cross section. Scale bars: 5 μm and 0.5 μm (inset). (**C**) Pixel-based colocalization analysis scatter plot confirms anti-correlation of DAPI and EU signals. PC: Pearson correlation coefficient; M1/M2: Manders' correlation coefficients DAPI vs. EU and EU vs. DAPI, respectively. (**D**) Line profile of signal intensity for both DAPI and EU from a representative euchromatic region 2 in panel (B), highlighting the mutually exclusive volumes occupied by DNA and RNA that are in the size range of 200-300 nm. (**E**) Single FIB-SEM section of a cryo-fixed HeLa cell, stained with osmium and uranyl acetate under cryo-conditions before resin embedding and imaging. Consecutive 4 nm section were cut by a focused ion beam (FIB) in orthogonal direction to growth surface and scanning electron microscopy (SEM) was recorded with 4 nm pixel size. The nuclear volume indicates G1 (or early S phase) stage. Scale bar: 5 μm. Below: inset magnifications of two indicated boxes with postulated features annotated. Red arrowheads indicate sites of nuclear pore complexes (NPCs) within the double membrane of the nuclear envelope. Blue asterisks indicate 200-300 nm wide aggregates of 10-20 nm diameter sized dark dots, likely nucleosomes. Orange arrowheads indicate ribosomes at the outer nuclear membrane. Blue arrowheads indicate putative linker segments of single nucleosomes. Scale bars: 0.5 μm inset 1 and 2 and 100 nm inset 3. (**F**) Columns 1-3: lateral cross section of the dataset shown in panel E followed by machine learning assisted segmentation of chromatin and putative RNPs. Columns 4-6: Average intensity projection of 80 consecutive segmented FIB-SEM sections covering a 320 nm z-range followed by 3D-Gauss filtering to match 3D-SIM's spatial resolution, closely resembles 3D-SIM micrograph at the same magnification. Scale bar: 0.5 μm. See also Fig. S2.

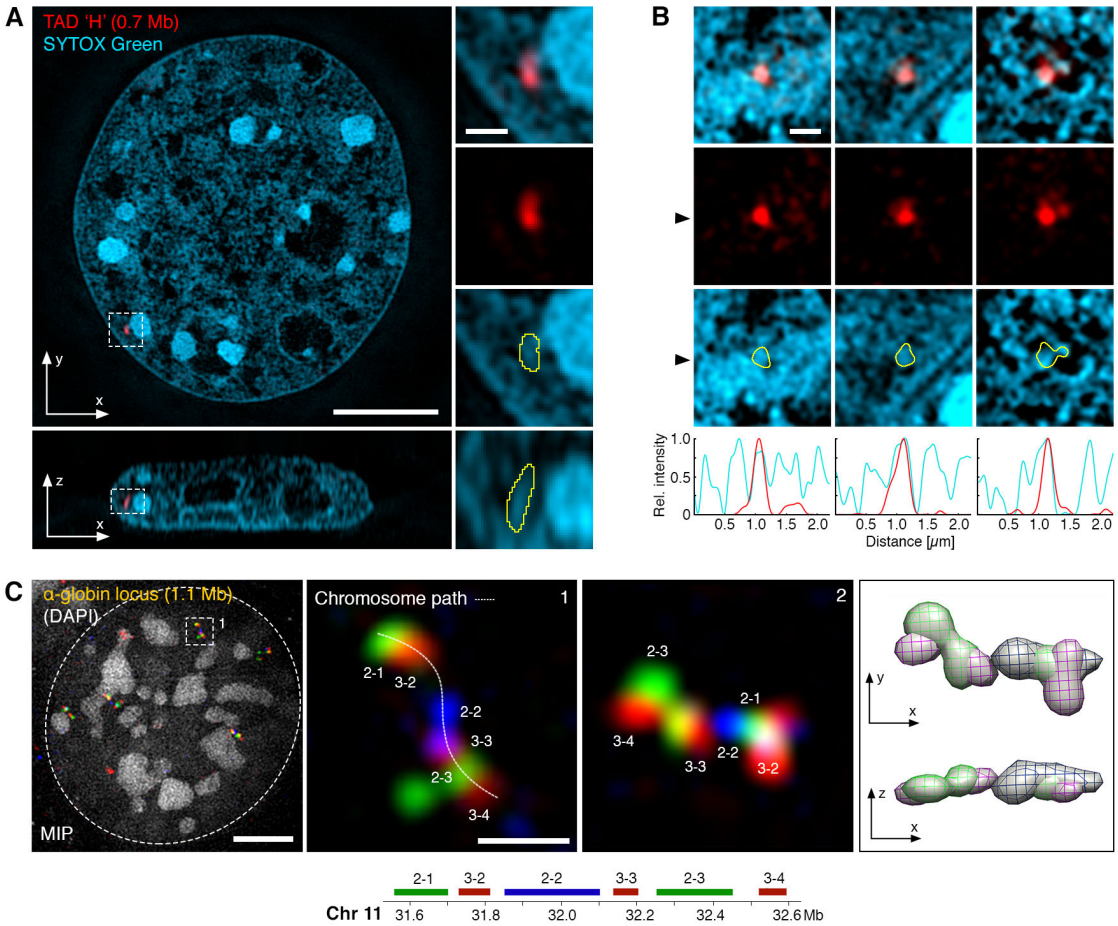

Fig. 2. Spatial relationship between CD chain and TADs. (**A**) RASER-FISH detection of a 0.7 Mb X chromosomal TAD 'H' (red; Hi-C map shown in Fig. S4A) and SYTOX Green whole chromatin labelling (cyan) in a mouse C127 cell imaged by 3D-SIM. Right, inset magnifications and below, orthogonal cross section. Yellow outlines of the FISH signal highlight ta close overlap with underlying CD chain nodes. (**B**) Further representative examples of TAD 'H' FISH signals from separate cells outlined against chromatin. Below, line profile of signal intensity for both TAD H (red) and SYTOX Green (cyan) calculated from a horizontal cross section at the black arrowhead. The spatial boundary of TAD H correlates strongly with CD boundaries. See also Fig. S4A, B. (**C**) Multicolor RASER-FISH labelling of sequential TADs across the α-globin gene locus detected in mouse C127 cells. Maximum intensity projections (MIP) of 3D-SIM micrographs show the genomic order of the probes is preserved as a curvilinear chain of discrete CDs in space. Note that DAPI has only low affinity for single-stranded DNA and is only used here to indicate the nuclear outline. A second example region from a different cell is shown on the right as MIP and 3D rendering (with views from different angles). Scale bars: 5 μm and 0.5 μm (insets). See also Fig. S4C.

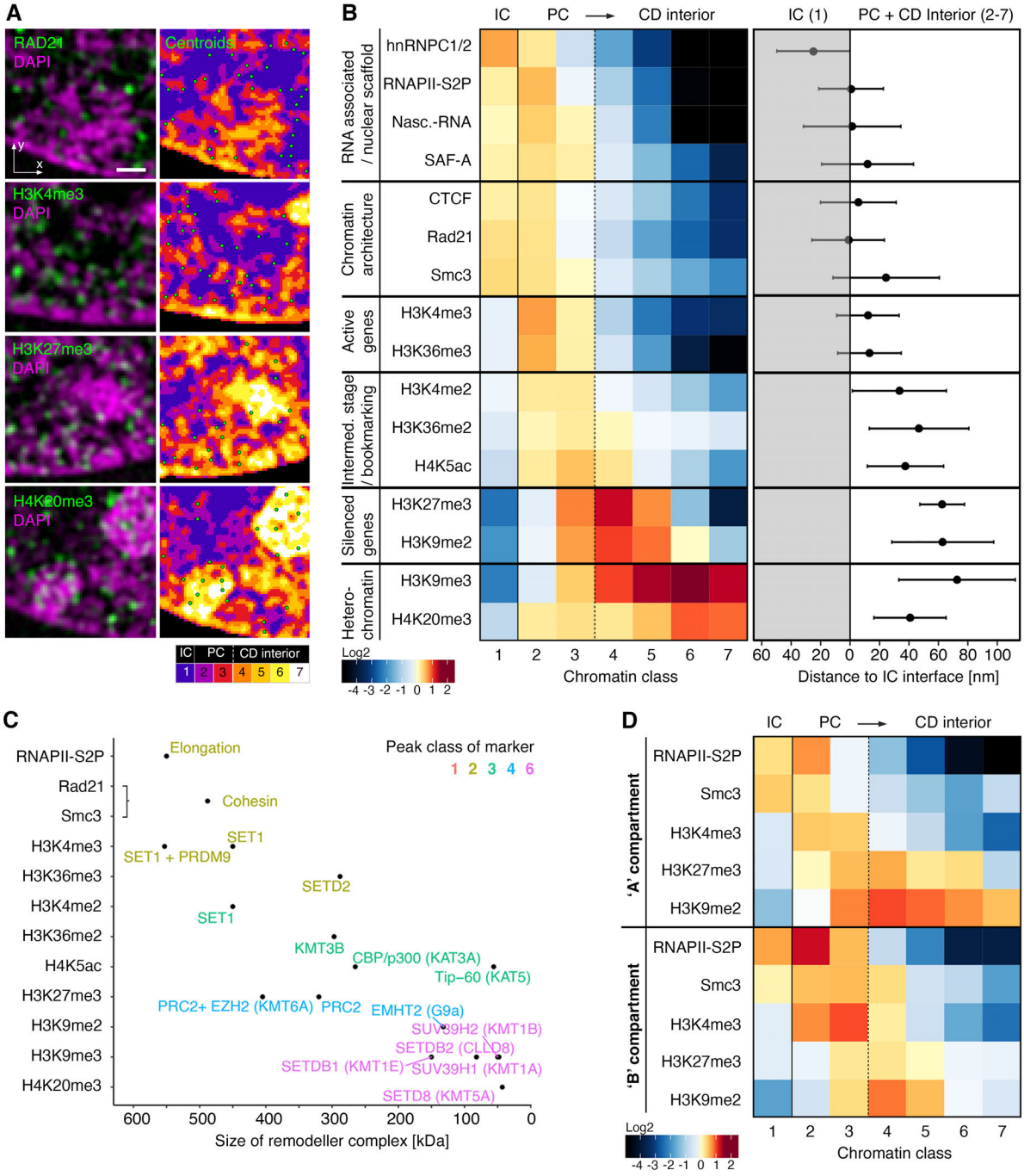

Fig. 3. Functional marker distribution in somatic cells reveals nanoscale 3D zonation correlated with protein complex size. (**A**) Left, representative sub-regions of single z-planes of 3D-SIM image stacks of mouse C127 cells in G1comparing the spatial localization of different markers with respect to chromatin. Right, marker centroid coordinates are depicted as green dots with a black outline. Note that centroids are determined with sub-voxel accuracy and may be closer to adjacent z-sections, and thus not be displayed in the chosen plane. G1 cell cycle stage was confirmed by the absence of EdU incorporation and relatively small nuclear volume. Scale bar: 0.5 μm. (**B**) Left: Heatmap of enrichment or depletion of IF signals relative to a random distribution (plotted in log2-fold change) for each chromatin class for each marker. Right: Distance to the IC interface for all markers. The mean distance and 95% confidence interval of the population are shown. At least 20 cells in

2 replicates were recorded for each marker, in total $N = 433$ cells. (**C**) Molecular weights of chromatin complexes corresponding to each marker. Scatterplot highlights an inverted correlation of size and preferential marker distribution (peak chromatin class color-coded). MW for cohesin was calculated from Smc1, Smc3, Rad21 and SA1/2. (**D**) Heatmap of relative IF signal distributions of representative markers in nuclear sub-volumes harboring mainly heterochromatin characteristic of B compartments (the segmented perinuclear rim and chromocenter regions), or euchromatin characteristic of A compartments (the remaining volume). Both compartments show a relatively conserved zonation pattern despite the different composition of chromatin in either region (Fig. S5D). Total number of cells $N = 170$.

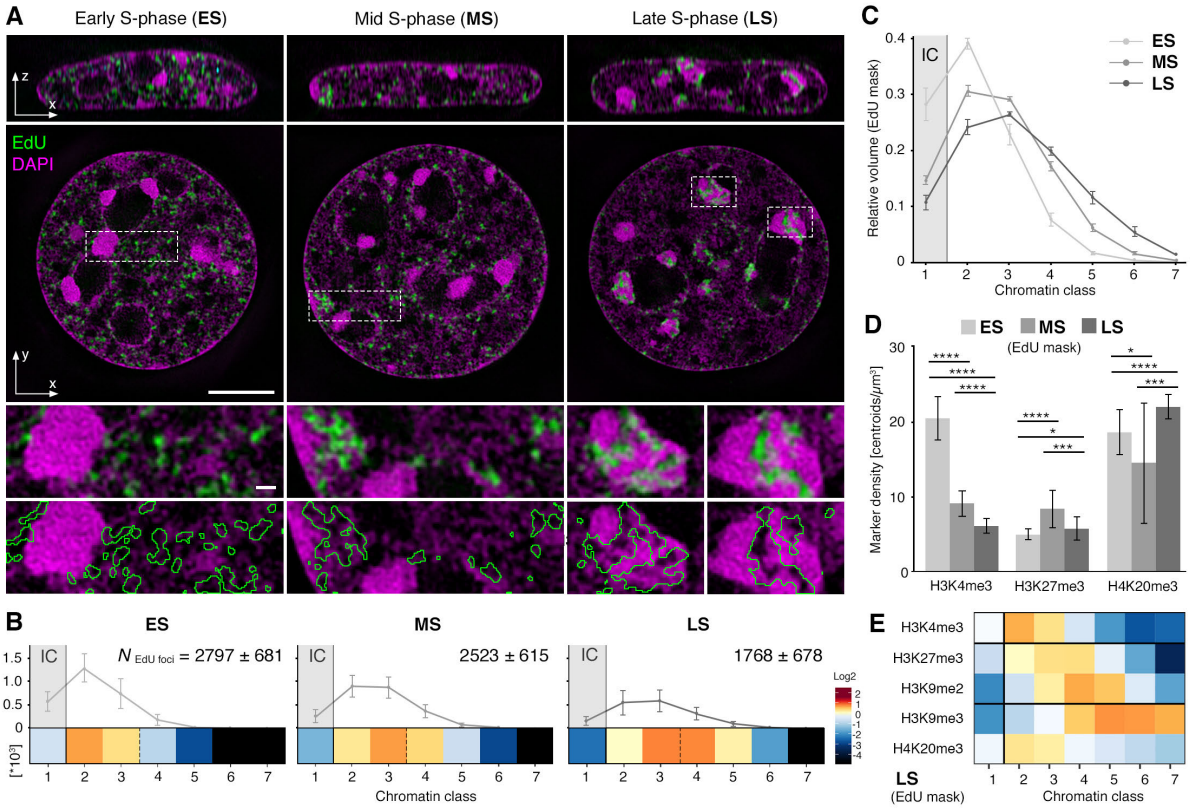

Fig. 4. Effect of active replication on chromatin composition. (**A**) Orthogonal and lateral cross sections of representative 3D-SIM datasets showing the chromatin landscape with the different patterns of replication foci (green) during S-phase progression from early, mid and late S-phase stages (left to right). Chromatin is stained with DAPI and replication is labelled using 15 min of EdU incorporation. Local replication regions were masked based on the EdU signal and outlined in green. Scale bar: 5 μm and 0.5 μm (insets). (**B**) Quantification of the absolute number of detected EdU foci in each of the different chromatin classes. The total number of EdU foci per cell is indicated as mean ± SD. Per S-phase stage, a heatmap of enrichment or depletion of EdU signals relative to a random distribution (plotted in log2-fold change) is depicted. (**C**) Proportion of chromatin classes (full nuclear volume segmented as shown in Fig. S5E) within EdU submask volumes in different S-phase stage. The mean ratios ± SD are depicted. (**D**) Foci number per μm^3 of EdU submask volume for the depicted histone modification in each condition, per S-phase stage. Mean ± SD are depicted. Number of cells: ES = 225, MS =227, LS =230. Significance value P: **** ≤ 0.0001; *** ≤ 0.001; * ≤ 0.05. (**E**) Heatmap of statistical distribution of selected marker in EdU masked regions of late S phase cells highlights a relaxation of repressive marker confinement to CD chain interior compared to G1 shown in Fig. 3B. See also Fig. S7 for a complete list of marker distributions in all cell cycle stages.

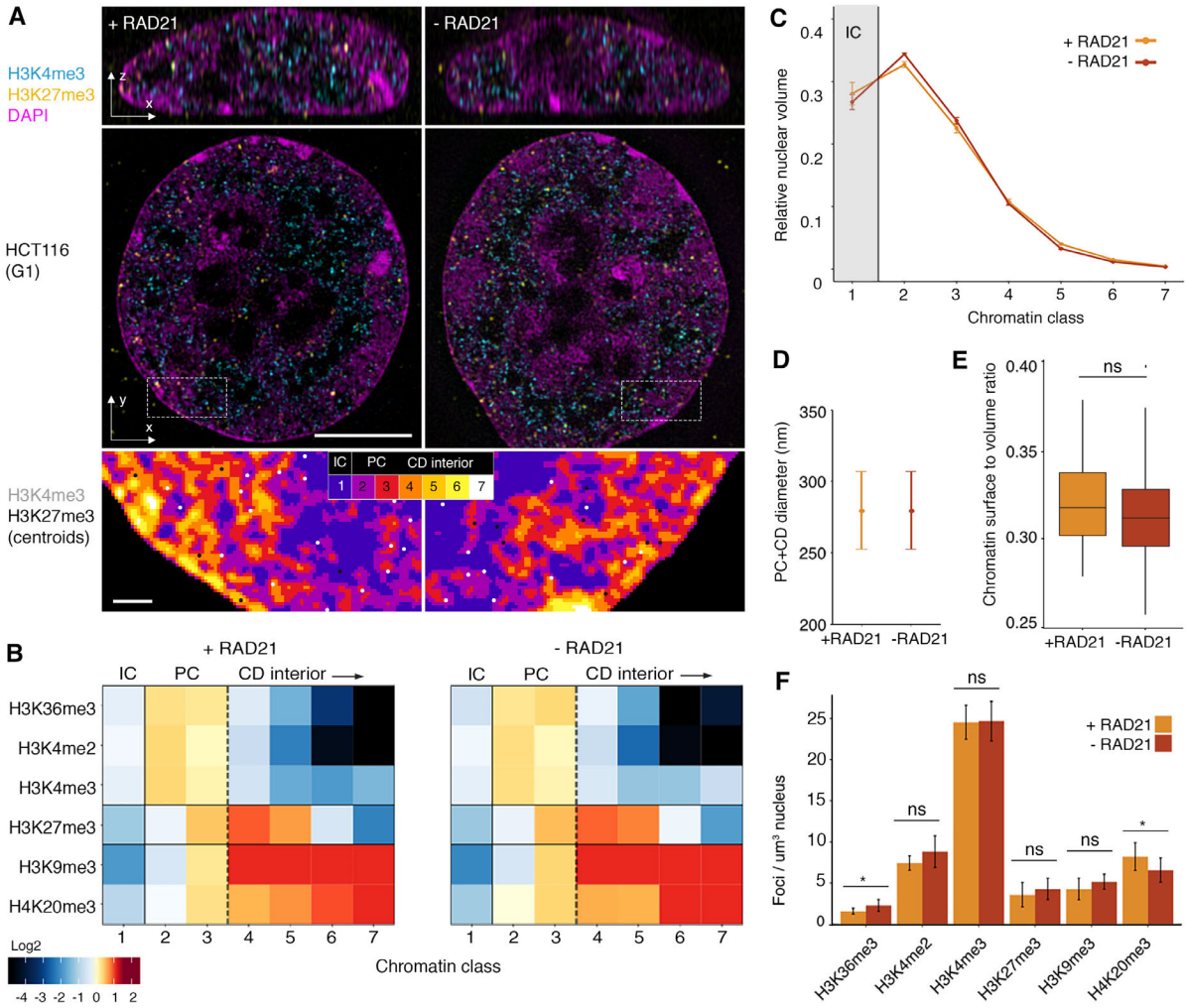

Fig. 5. Epigenome zonation persists after cohesin ablation. (**A**) Representative single z-planes of 3D-SIM images comparing the chromatin landscape in human HCT116 in the presence of cohesin, and without cohesin. Control cells were only treated with auxin for 6 h (+RAD21, left) or RAD21 ablated cells after 16 h doxycycline and 6 h auxin treatment (-RAD21, right). Insets show the segmented topography with the spatial distribution of H3K4me3 and H3K27me3 represented as white and black dots respectively. Scale bars: 5 μm and 0.5 μm (insets). See also Fig. S8A, B. (**B**) Heatmap of enrichment or depletion of IF signals from a representative subset of histone modifications. Respective profiles for individual markers with error bars show no significant change for any distribution See also Fig. S8C. (**C**) Proportion of nuclear volume for each class, showing no significant change after ablation of cohesin function (mean ±95% CI). (**D-E**) Quantification of the PC+CD dimensions (D, ±95% CI, see Methods) and IC-PC surface area to PC+CD volume ratio (E, ±SD) shows no significant change between RAD21 positive or depleted conditions. (**F**) Quantification of the mean number of foci detected for each condition shows almost no changes between RAD21 positive or depleted conditions (±SD). Total number of cells: + RAD21= 80; - RAD21= 104. Significance values P: * ≤ 0.05; non-significant ns > 0.05.

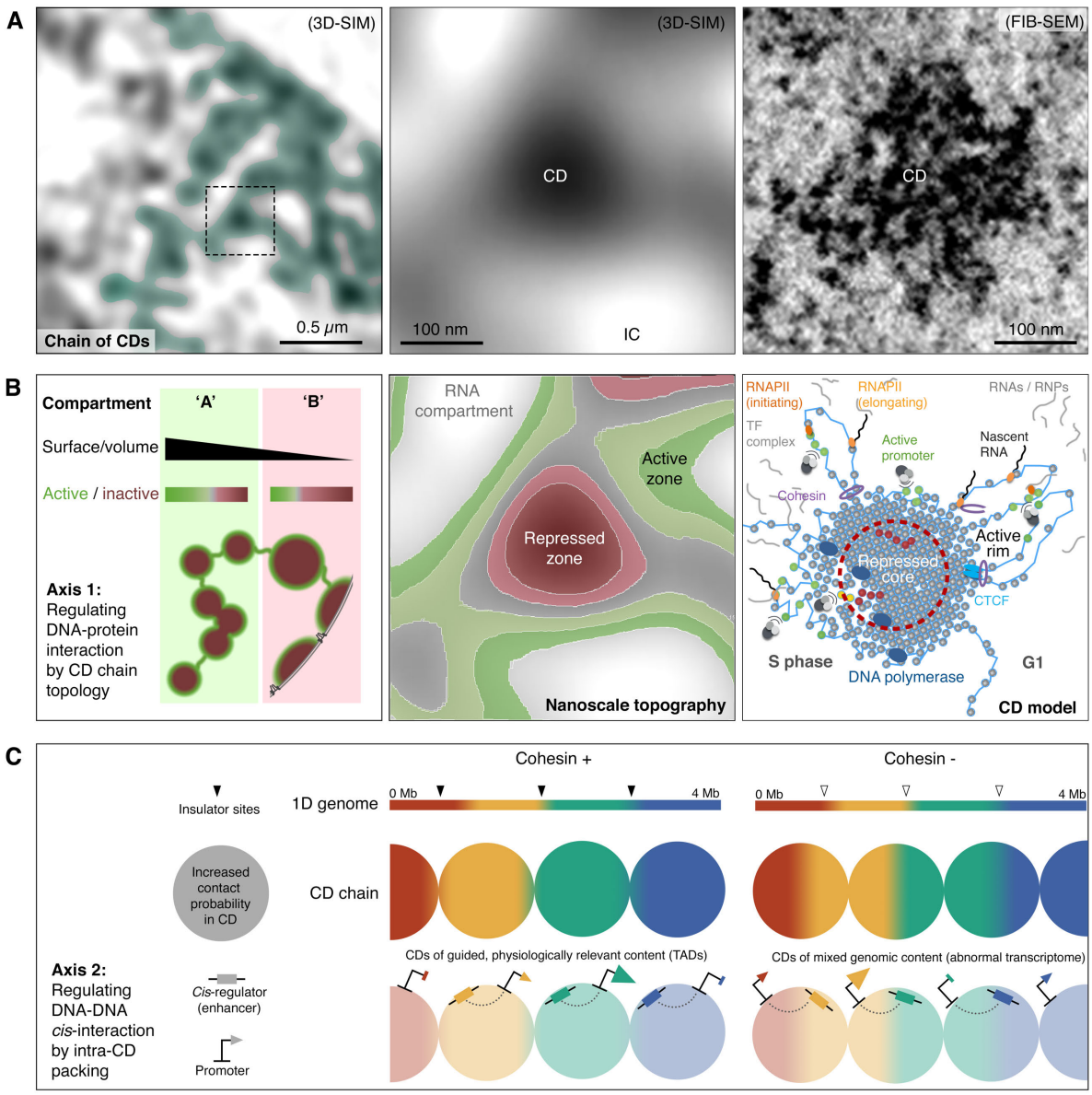

Fig. 6. Model of the interphase nucleus as a chain of CDs from the mesoscale to the nanoscale. (**A**) Left: Super-resolved interphase chromatin stained with DAPI in a C127 cell, with an overlaid representation of a putative curvilinear chain of CDs. Center: Zoom-in to an individual CD, indicated by the black dashed box in the left panel, imaged by 3D-SIM. Right: an equivalently-sized individual CD imaged by FIB-SEM. (**B**) Model of functional zonation at each scale or resolution for images in panel A. Left: The ratio of active surface area to volume (SA/V) for DNA-protein interactions is the first regulatory axis of CDs over genome activity. Differing ratios of SA/V in either A or B compartments reflects changes in CD chains, and gives rise to generally active or inactive compartments. In this cartoon the 'B' compartment is adjacent to the lamina, represented by a black line interrupted by nuclear pores. Center: Preferential zonation of various functions occurs at the nm scale, relevant to single CDs. Right: The nanoscale zonation can be modelled by the radial position of histones with diverse PTMs and protein complexes. Almost no active markers are detected beyond ~60 nm from the PC-IC interface towards the CD core, such that any silenced promoter (red spots) at this 'depth' (within red dashed circle) may remain inactive by being

inaccessible to the transcriptional machinery rather than through active deposition of repressive histone PTMs. Nevertheless, in S phase the local decompaction caused by DNA polymerase offers the chance for certain loci to escape inactivation, by being released from their inaccessible state (yellow spots). (**C**) Supporting appropriate DNA-DNA interactions is the second regulatory axis of CDs over genome function. The presence of cohesin links the 3D structure to the correct 1D genomic context, leading to physiologically relevant interactions observed as 'TADs' in population Hi-C maps (left). Folding of the genome into biophysically defined CDs in the absence of cohesin leads to CD structures without physiological relevance (multiple colors mixed over genomic insulator boundaries, right).